Sensors & Transducers, Vol. 229, Issue 1, January 2019, pp. 47-54

www.sensorsportal.com

Sensors & Transducers

Published by IFSA Publishing, S. L., 2019
http://www.sensorsportal.com

Gamma Ray and Neutron Sensors for Remote Monitoring Using Aerial Robotic Platforms

Monia KAZEMEINI, Alexander BARZILOV, Woosoon YIM and Joon LEE

University of Nevada, Las Vegas, 4505 S. Maryland Parkway, Las Vegas, NV 89154, United States
Tel.: +17028954325, fax: +17028953936
E-mail: kazemei2@unlv.nevada.edu

Received: 30 November 2018 /Accepted: 31 December 2018 /Published: 31 January 2019

Abstract: Remote radiation sensing technologies are essential for radiation safety and environmental security measures. The use of unmanned aerial systems equipped with gamma-ray and neutron sensors enables monitoring of ionizing radiation in hard to reach hazardous zones where the contamination is unknown. To keep personnel away from the radiation exposure by using remote measurement techniques, these sensors should be integrated into robotic platforms, and the analysis of sensor's signals should be automated and carried out onboard. Two sensors were integrated into an octocopter aerial platform to address this need: a semiconductor Cadmium Zinc Telluride gamma-ray sensor and an elpasolite $Cs_2LiYCl_6:Ce^{3+}$ scintillator based gamma/neutron sensor. To allow easy deployment in the field, both radiation sensors were designed as plug-and-play components using the Robot Operating System for onboard processing of the sensor's data and for fusion of the processed data with the real time kinematic GPS information.

Keywords: Remote sensing, Unmanned aerial system, Gamma spectroscopy, Neutrons, CZT, CLYC, Plug-and-play sensors.

1. Introduction

To address environmental safety and radiation protection matters, it is important to evaluate the radiation contamination in areas which may be hazardous for personnel and hard to reach. The ionizing radiation sources can be displaced or lost [1-2] causing contamination of infrastructure and the dose delivered to public. Radioactive materials can be released into the environment as a result of technical accidents at nuclear facilities or natural cataclysms that cause such accidents. For example, the accident at the Fukushima Daiichi nuclear power plant led to radiological contamination of the plant's infrastructure and adjacent regions, including the wide area water pollution [3]. Radiation monitoring using robots equipped with the navigation means makes it possible to assay these zones, while reducing the radiation exposure risk to operators.

Using unmanned aerial systems (UAS) as robotic platforms, gamma-ray and neutron sensors can be deployed for remote measurements in the field conditions [4-5]. Aerial robotic systems allow for the radiation sensor's data to be dynamically tracked enabling further analysis of the radiation flux in the time and space domains [6-7]. UAS can be used for mapping of unsafe regions [8-10] in order to increase the situational awareness of the personnel. Multiple UAS platforms can be also utilized for the cooperative sensing tasks: for example, for contour mapping of boundaries of the hazardous zones and for the search of unattended sources [11]. In order to undertake

UAS-based radiation sensing operations, sensors should be integrated into aerial platforms. The sensor's integration into the UAS should not impact the battery lifetime. In addition, operators should be able to 'hot' plug and unplug the sensors into a robotic platform in the field conditions [12].

Analysis of the measured sensor's signals should be carried out using an onboard UAS computer taking into account its limited data processing capabilities. Besides, this approach helps to decrease the size of data packages that are transmitted from the aerial system to a ground station, or to other UAS platforms [13].

To address these needs, two sensors were designed as the 'plug and play' integral components of the UAS: a $Cs_2LiYCl_6:Ce^{3+}$ (CLYC) based scintillation sensor for simultaneous neutron and photon measurements and a Cadmium Zinc Telluride (CZT) semiconductor based sensor for high resolution gamma ray spectrometry. Both sensors can work under ambient temperature conditions without cryogenic cooling which is essential for the field applications.

2. Radiation Sensors

2.1. Scintillation Neutron and Photon Sensor

CLYC is a scintillation material [14] that allows for simultaneous neutron and photon measurements. The density of this elpasolite compound is 3.31 g/cm^3. The scintillation light produced by the CLYC has a wavelength range 275 nm - 450 nm (the peak is at 370 nm). At the 405-nm light wavelength, the CLYC's refractive index is 1.8.

The scintillation properties of elpasolites enable gamma-ray spectrometry [15]. It produces 20 thousand scintillation photons under the incident gamma rays (per 1 MeV). Neutrons are detected using CLYC via $^6Li(n,\alpha)^3H$ nuclear reaction with the emission of energetic charge particles; 70 thousand scintillation photons are generated in the crystal per one thermal neutron. The excitation of a CLYC crystal caused by a gamma-ray is followed with two decay processes: the core-to-valence (CVL) decay (1-ns decay constant) and the prompt cerium decay that has 50-ns decay constant. A neutron induced excitation of the CLYC is followed with a cerium self-trapped excitation that has the 1 μs decay constant. Due to the different decay times after neutron and photon excitations, CLYC makes it possible to segregate signals caused by these two radiations using the neutron/photon pulse shape discrimination (PSD) techniques [16].

The sensor module was designed using a 2.54-cm diameter, 2.54-cm long cylindrical CLYC crystal coupled with an optical readout - a super bialkali photomultiplier tube (PMT) appropriate for the wavelength range of CLYC's scintillation light. A silicon photomultiplier (SiPM) can be also used for detection of the scintillation. The PMT was equipped with a high voltage generator that was connected to a small-sized emorpho digitizer. The scheme of the CLYC sensor is shown in Fig. 1. The components of the sensor were packaged in a plastic housing designed to be easily attached to the UAS. The assembled sensor module is shown in Fig. 2.

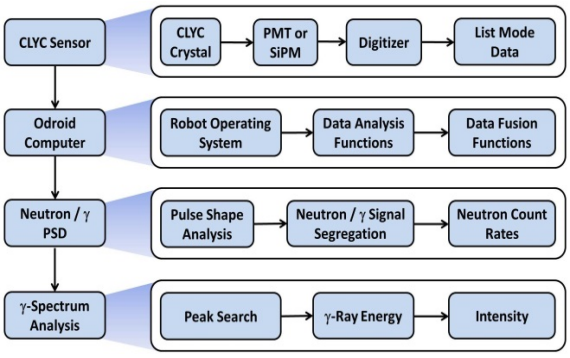

Fig. 1. Block diagram of the CLYC sensor.

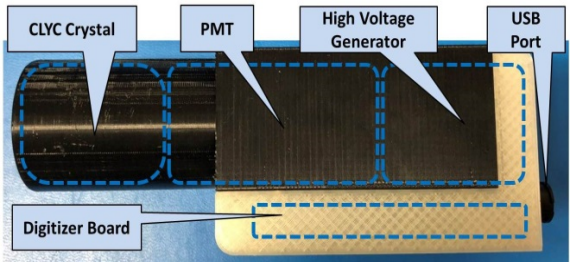

Fig. 2. CLYC sensor module.

After absorption of a CLYC's scintillation photon in the PMT's photocathode, an electron is ejected and directed by the focusing electrode in the direction of a set of dynodes which multiply electrons via the secondary emission. The resultant PMT's current signal is digitized by the emorpho. The recorded waveforms of neutron and photon induced signals of the CLYC sensor are shown in Fig. 3(a). The waveform is processed providing in a list mode the following three values: a timestamp, integral under the signal curve (proportional to the energy of radiation) calculated using the user defined integration time (IT), and integral under the beginning part of the signal assessed using a pre-set partial integration time (PIT). The USB cable was used to connect the digitizer to the UAS computer Odroid-XU4 running Ubuntu Linux and Robot Operating System (ROS) [17]. ROS is designed as a framework for robotic applications and includes libraries and tools. It consists of a number of nodes communicating with each other using a publishing or subscribing messaging model.

The list mode data was used for the neutron/gamma PSD analysis. A PSD value was calculated as a ratio of the areas under the tail part and the front part of the signal. Larger PSD values are associated with the neutron waveforms that exhibit

longer tails that the photon waveforms. The PSD value was used to segregate waveforms into two groups (neutron events and photon events).

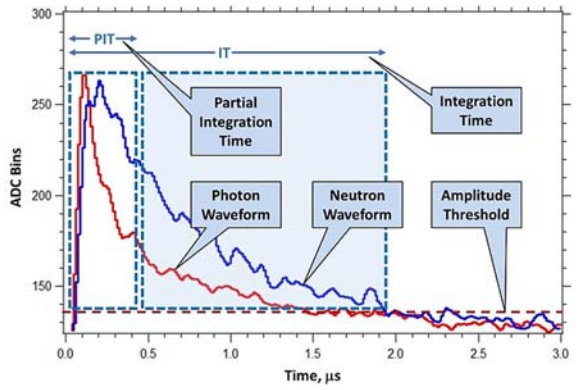

(a)

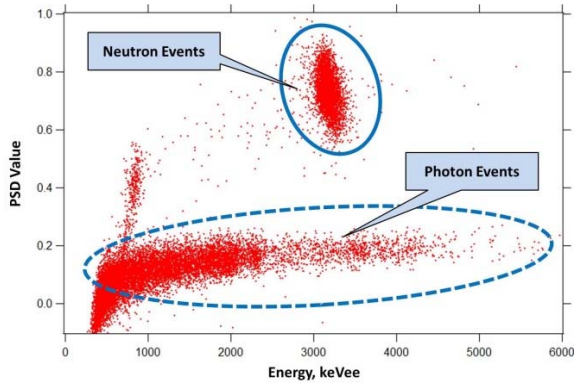

(b)

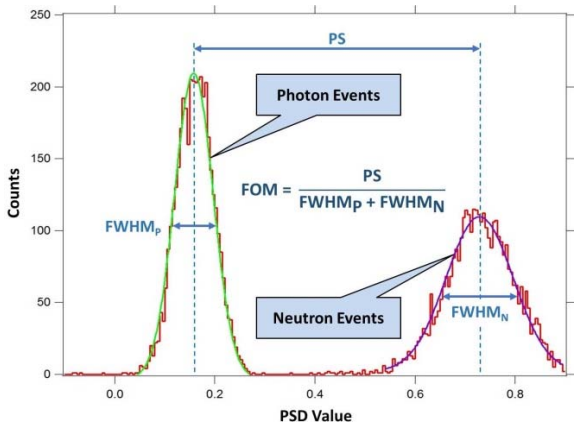

(c)

Fig. 3. (a) Digitized waveforms of neutron and gamma ray induced signals of the CLYC sensor; (b) Neutron/photon PSD plot; (c) Measurement of the PSD figure of merit.

Results of CLYC's neutron/gamma PSD measurements using a PuBe (α,n) source are shown in Fig. 3(b). The neutron event dots are centered around the 3200 keV value (electron equivalents, keVee). This plot illustrates good separation of neutron and photon events. A PSD figure of merit (FOM) [18] for CLYC was measured using a plot of sensor's counts versus PSD values: the peak separation was divided by the sum of full widths at a half maximum (FWHM) of neutron and photon peaks yielding a value of 2.3 (Fig. 3(c)). This PSD algorithm was coded using C as a function in ROS.

The gamma-ray signals, segregated from neutron signals, were used to generate a photon energy distribution. The spectrum of photons emitted by a ^{137}Cs source measured using the CLYC sensor is shown in Fig. 4. The measured FWHM photon energy resolution of the sensor is 5 % at 662 keV, 3.6 % at 1173 keV and 3.3 % at 1332 keV.

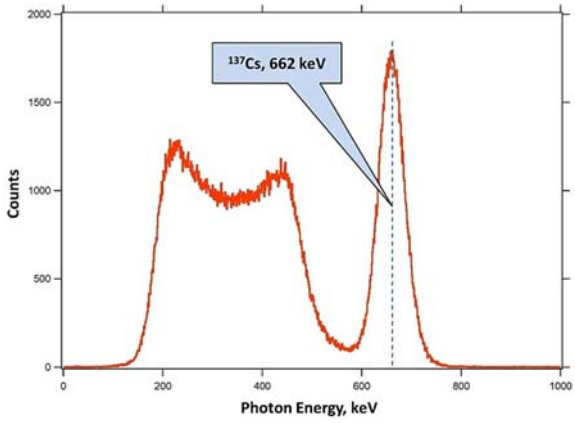

Fig. 4. Photon spectrum of a ^{137}Cs source measured using the CLYC sensor.

The photon spectrum should be analyzed in order to find peaks and with their centroids and intensities. This information enables identification of gamma emitters with their yields. Various computational techniques were studied spectral analysis [19-21]. Due to limitations of the UAS computer, a robust peak identification algorithm based on Mariscotti's technique [22] was developed as a function within ROS. Peaks were approximated using Gaussian functions. The photon peak's 'background' was approximated using a linear function within several peak widths. Number of counts in a channel i was calculated as

$$C(i) = \varphi(i) + A \cdot i + B, \qquad (1)$$

where A and B constants describe the spectrum background. $\varphi(i)$ in (Eq. 1) is the Gaussian function:

$$\varphi(i) = H \cdot exp(-\{i-h\}^2/\{2 \cdot \sigma^2\}), \qquad (2)$$

where H is the height of the peak with centroid at a channel h. In (Eq. 2), σ is set as $FWHM_{peak}$ / 2.355. Peak is located if a second derivative of $C(i)$ is not zero. Because spectra were recorded as discrete datasets $N(i)$, a centered finite-divided difference approximation was used for the second derivative:

$$\ddot{C}(i) = \{N(i+1) - 2N(i) + N(i-1)\}/\Delta^2, \qquad (3)$$

where Δ is a step of the energy scale. Because spectral data have statistical fluctuations, the spectrum was smoothed by calculating an average of $C(i)$ values for ξ channels near the i channel. This process was reiterated ψ times yielding a smoothed spectrum:

$$C_i^{sm}(\psi, \xi) = \sum_j W_{ij}(\psi, \xi) N_j, \quad (4)$$

where W_{ij} are the weighting factors. Parameters ψ, ξ, and W_{ij} were set for the CLYC sensor to resolve peaks of desired height. Nonzero second derivatives of the smoothed $C^{sm}(i)$ dataset (Eq. 4), approximated using (Eq. 3), were utilized to locate peaks. This approach enabled distinguishing full-energy peaks from Compton shoulders, providing peak's centroids and intensities (the area under the Gaussian). This algorithm was coded using C language as a function within ROS.

2.2. Semiconductor Gamma Ray Sensor

The GR1A module [23] was used to design a UAS-based CZT sensor for high resolution gamma-ray spectroscopy. CZT detectors are able to process more than ten million photons per square millimeter [24]. The scheme of the CZT sensor is shown in Fig. 5. The module's dimensions are 2.5 cm × 2.5 cm × 6.1 cm. The module weight is 49.2 grams. It encloses a 1 cm^3 CZT crystal equipped with a preamplifier, shaper, multichannel analyzer (MCA, 4096 channels), baseline restorer, and high voltage supply. The CZT sensor is powered via USB from the onboard computer (power consumption is less than 250 mW), so additional power is not required.

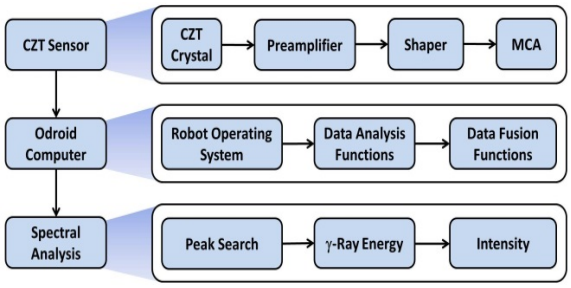

Fig. 5. Scheme of the CZT sensor.

Once gamma radiation interacts with the CZT, electron hole pairs are created, moving in the electric field. The resulting current signal is sent to the preamplifier, where the voltage pulse is created. Then the shaping amplifier converts the signal to a Gaussian shaped waveform. The MCA generates the photon spectrum. The CZT sensor is shown in Fig. 6. Its energy range is 30 keV - 3 MeV. The CZT's FWHM energy resolution was measured to be less than 2 % at 662 keV (Fig. 7), which is essential for identification of gamma emitters.

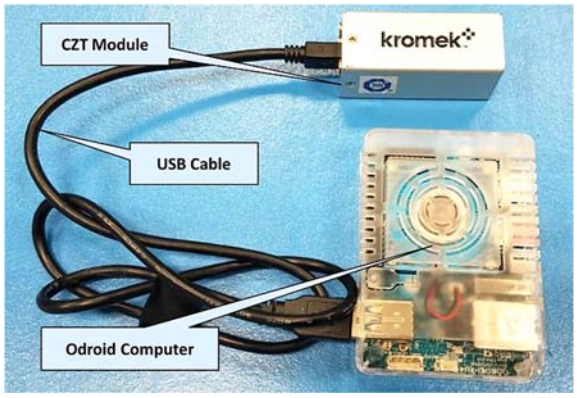

Fig. 6. CZT sensor connected to Odroid via a USB cable.

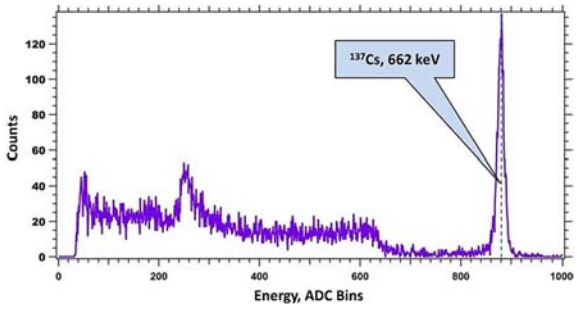

Fig. 7. Photon spectrum of a ^{137}Cs source measured using the CZT sensor.

The ROS function for the photon spectrum analysis described in Section 2.1 was utilized for the CZT sensor as well (ψ, ξ and W_{ij} in the algorithm were modified for a high-resolution spectrum).

3. Sensor Integration into a UAS

CLYC and CZT sensors were integrated into the UAS platform - the DJI S1000 octocopter [25] (Fig. 8). This UAS is powered by 6S Lithium batteries. Its takeoff weight is up to 11 kilograms. It can fly during 15 minutes. The UAS's landing gear can be raised in flight.

Fig. 8. UAS with the CZT sensor attached to the platform.

The diagonal wheelbase of the octocopter is 1045 mm with 386-mm frame arm length, and 380-mm propeller dimension. As a UAS flight controller, the Pixhawk 2.1 [26] was used. It contains an isolated and dampened inertial measurement unit (IMU). The built-in IMU heating system enables operations below 0°C. Moreover, it has robust interface connectors improving the shock resistance and diminishing the noise. It reduces interference to the sensors with the separate IMU and flight management unit (FMU) system.

The plug-and-play approach was used for the sensor integration into the aerial platform. It supports 'hot plugging' and 'hot unplugging' of sensors into the USB interface of UAS. An operator does not have to set up the sensor's parameters each time the octocopter is powered on.

When a sensor is plugged in and powered on, the operating system (OS) identifies the sensor type. Then OS installs a driver for this sensor, and a measurement process is initiated. The measured sensor's data is processed, analyzed, and published. A block diagram shown in Fig. 9 illustrates the plug-and-play operation within ROS allowing for the management of sensors.

The radiation data generated by sensors were time stamped and fused with the UAS's position data based on the Real Time Kinematic (RTK) GPS positioning technology. The RTK GPS is a navigation technique that enhances the precision of position data derived from satellite-based positioning systems. It is based on measurements of the phase of the signal's carrier wave using a single reference station to provide the real time corrections [27-28].

The RTK GPS operational diagram is shown in Fig. 10. The base station with surveyed coordinates has a fixed Swift Duro GPS Receiver. The UAS platform carries a single board computer, Piksi Multi GPS Receiver, and L1/L2 GPS antenna [29]. Correction data for ionospheric error calculations was transmitted to the GPS Receiver of the UAS platform from the base station. The RTK GPS has the following characteristics: raw data measurement rates up to 20 Hz, RTK position outputs up to 10 Hz. To test performance of RTK GPS for UAS, the fixed-position base station and four RTK 'rovers' were setup as shown in Fig. 11(a).

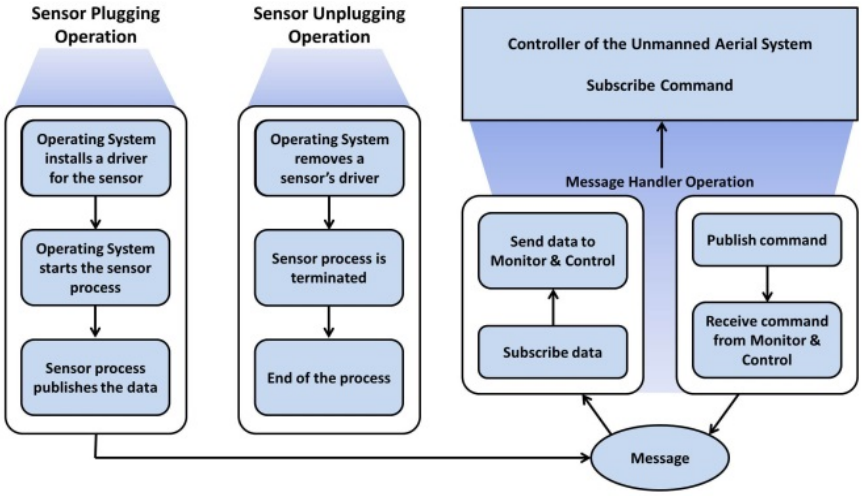

Fig. 9. Sensor's plug-and-play operation scheme.

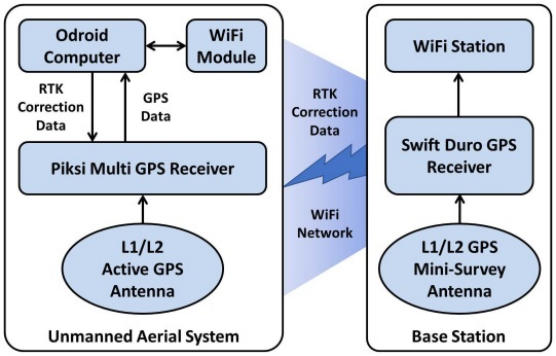

Fig. 10. RTK GPS operational diagram.

The RTK GPS antennas of four rovers were equally spaced - 20 cm between the antennas as shown in Fig. 11(b). The Odroid computers were running Ubuntu OS, ROS, and the application programing

interface to access GPS data. The measured GPS position data with RTK correction are shown in Table 1. The baseline position is related to coordinates of the base station. Standard deviation σ (68 % probability) of the position of four GPS units was estimated as 2.5 mm, and 5.5 mm for the altitude. The UAS position and altitude data measured using the RTK GPS technology with such accuracy enables high fidelity mapping of sensor's radiation data, and allows using it in cooperative sensing scenarios that involve multiple UAS.

The data fusion function programmed in C within ROS, adds the UAS coordinate and altitude information at the time of measurement to the time stamped CLYC or CZT sensor data. Fig. 12 illustrates plug-and-play operation of the CZT sensor. When the sensor is hot plugged via the USB cable in the single board Odroid-XU4 computer running Ubuntu and ROS with custom data analysis and fusion functions, the OS starts the CZT sensor's driver process shown in the process status window. The sensor records the radiation data that are captured. The captured raw data from the CZT sensor for a measurement using a ^{137}Cs gamma source are then plotted to display the gamma-ray spectrum.

The captured raw data are processed using the data analysis functions within ROS, segregating neutron and photon counts (CLYC sensor) and extracting the gamma peak energy and intensity data (CLYC and CZT sensors). Fig. 13 illustrates data fusion for the CLYC sensor.

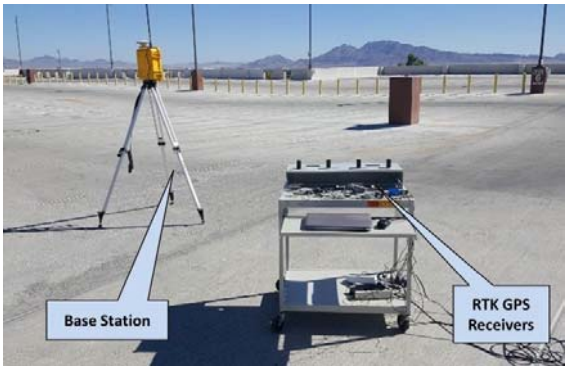

(a)

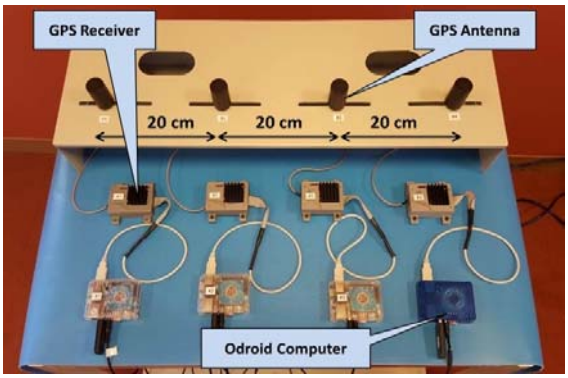

(b)

Fig. 11. (a) Testing RTK GPS sensors; (b) GPS antennas and receivers connected to computers.

Table 1. GPS position data with RTK (scale: mm).

GPS	Baseline North Average	Baseline East Average	Baseline Altitude Average	Baseline North St. Dev. σ	Baseline East St. Dev. σ	Baseline Altitude St. Dev. σ
1	889.09	5,066.99	981.11	2.59	2.03	5.11
2	833.62	5,252.15	989.15	2.38	2.07	5.02
3	775.81	5,448.22	982.77	2.66	2.66	5.67
4	724.63	5,637.97	988.67	2.36	2.44	5.94

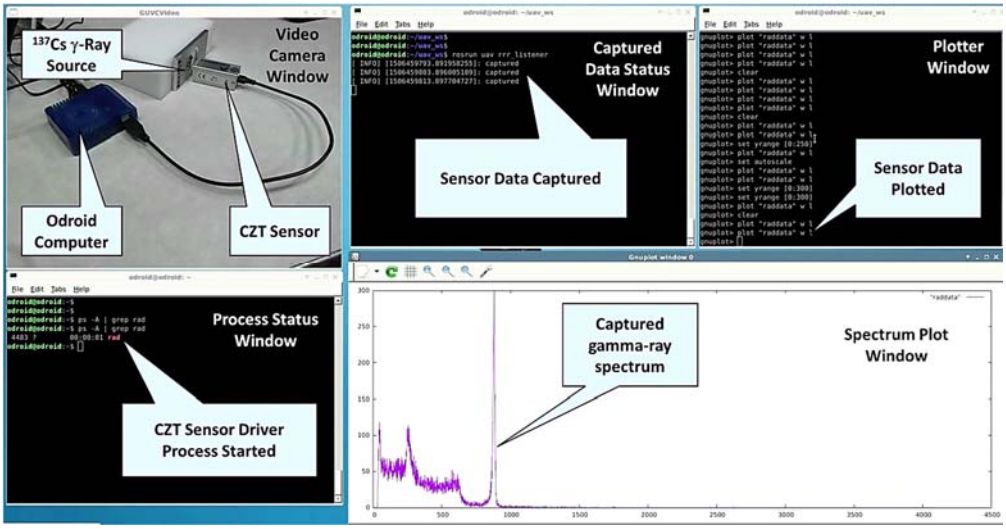

Fig. 12. Testing of plug-and-play operation of the CZT sensor.

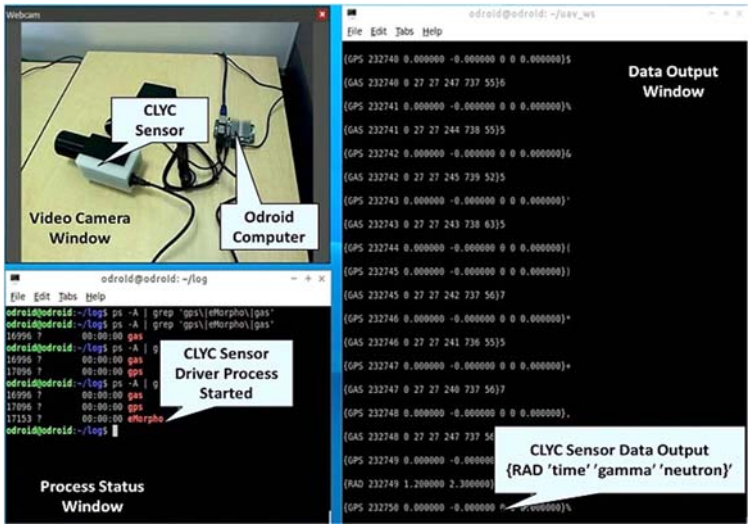

Fig. 13. CLYC sensor: the data fusion.

4. Conclusions

Cadmium Zinc Telluride and $Cs_2LiYCl_6:Ce^{3+}$ sensors were designed for the use with aerial robotic platforms. Neutrons and gamma rays can be simultaneously measured using the CLYC sensor with effective pulse shape discrimination of these two radiations. The CZT sensor was designed for high resolution gamma spectroscopy. Sensors were integrated onto the UAS using Robot Operating System as the plug-and-play components, allowing a user-friendly application in the field conditions. Data analysis and fusion functions were programmed within ROS. The time stamped sensor's data were merged with the RTK GPS information.

Acknowledgements

This work was supported by the Department of Energy Minority Serving Institution Partnership (MSIPP) managed by the Savannah River National Laboratory under SRNS contract MSIT00016.

References

[1]. J. Till, H. Grogan, Radiological risk assessment and environmental analysis, *Oxford University Press*, 2008.

[2]. R. Runkle, A. Bernstein, P. Vanier, Securing special nuclear material: recent advances in neutron detection and their role in nonproliferation, *Journal of Applied Physics*, Vol. 108, Issue 11, 2010, pp. 111101-1–111101-21.

[3]. K. Nagatani, *et al*., Emergency response to the nuclear accident at the Fukushima Daiichi nuclear power plants using mobile rescue robots, *Journal of Field Robotics*, Vol. 30, Issue 1, 2013, pp. 44-63.

[4]. J. Jin, *et al*., A switched-system approach to formation control and heading consensus for multi-robot systems, *Intelligent Service Robotics*, Vol. 11, Issue 2, 2018, pp. 207-224.

[5]. T. Sen, L. Moore, An organizational decision support system for managing the DOE hazardous waste cleanup program, *Decision Support Systems*, Vol. 29, 2000, pp. 89-109.

[6]. J. Hartman, A. Barzilov, I. Novikov, Remote sensing of neutron and gamma radiation using aerial unmanned autonomous system, in *Proceedings of the IEEE Nuclear Science Symposium and Medical Imaging Conference (NSS/MIC'15)*, San Diego, USA, 31 October - 7 November 2015, pp. 1-4.

[7]. J. Han, Y. Chen, Multiple UAV formations for cooperative source seeking and contour mapping of a radiative signal field, *Journal of Intelligent Robotic Systems,* Vol. 74, Issue 1-2, 2014, pp. 323-332.

[8]. J. Cook, M. Kazemeini, A. Barzilov, W. Yim, On-board radiation sensor and low-altitude contour mapping of radiation fields using UAS swarm, in *Proceedings of the Waste Management Symposium*, Phoenix, USA, 18 - 22 March 2018, pp. 1-12.

[9]. R. Raffard, *et al*., Distributed optimization for cooperative agents: application to formation flight, in *Proceedings of the IEEE Conference on Decision and Control*, 2004, pp. 2453-2459.

[10]. L. Arranz, *et al*., Translation control of a fleet circular formation of AUVs under finite communication range, in *Proceedings of the IEEE Conference on Decision and Control* (*CDC*), Shanghai, China, 15-18 December 2009, pp. 8345-8350.

[11]. P. Ogren, E. Fiorelli, N. Leonard, Cooperative control of mobile sensor networks: adaptive gradient climbing in a distributed environment, *IEEE Transactions on Automatic Control*, Vol. 49, 2004, pp. 1292-1302.

[12]. M. Kazemeini, A. Barzilov, W. Yim, J. Lee, Integration of CZT and CLYC radiation sensors into a UAS platform, in *Proceedings of the 4th International Conference on Sensors and Electronic Instrumentation Advances* (*SEIA'18*), Amsterdam, Netherlands, 19 - 21 September 2018, pp. 57-59.

[13]. M. Kazemeini, Z. Cook, J. Lee, A. Barzilov, W. Yim, Plug-and-play radiation sensor components for unmanned aerial system platform, *Journal of Radioanalytical and Nuclear Chemistry*, Vol. 318, Issue 3, 2018, pp. 1797-1803.

[14]. A. Giaz, *et al*., The CLYC-6 and CLYC-7 response to gamma-rays, fast and thermal neutrons, *Nuclear Instruments and Methods in Physics Research A*, Vol. 810, 2016, pp. 132-139.
[15]. P. Guss, T. Stampahar, S. Mukhopadhyay, A. Barzilov, A. Guckes, Scintillation properties of a $Cs_2LiLa(Br_6)90\ \%(Cl_6)10\ \%:Ce^{3+}$ (CLLBC) crystal, in *Proceedings of the SPIE Radiation Detectors - Systems and Applications Conference XV*, San Diego, USA, 19 - 21 August 2014, pp. 921505-1 - 921505-15.
[16]. N. D'Olympia N, *et al*., Pulse-shape analysis of CLYC for thermal neutrons, fast neutrons, and gamma-rays, *Nuclear Instruments and Methods in Physics Research A*, Vol. 714, 2013, pp.121-127.
[17]. Robot Operating System (ROS) (http://www.ros.org/).
[18]. J. Hartman, A. Barzilov, E. Peters, S. Yates, Measurements of response functions of EJ-299-33A plastic scintillator for fast neutrons, *Nuclear Instruments and Methods in Physics Research A*, Vol. 804, 2015, pp. 137-143.
[19]. A. Barzilov, B. Kessler, P. Womble, Analysis of 14-MeV neutron induced gamma-ray spectra using multiwavelets, *Radiation Measurements*, Vol. 79, 2015, pp. 43-49.
[20]. M. Medhat M. Artificial intelligence methods applied for quantitative analysis of natural radioactive sources, *Annals of Nuclear Energy*, Vol. 45, 2012, pp. 73-79.
[21]. A. Barzilov, P. Womble, Study of Doppler broadening of gamma-ray spectra in 14-MeV neutron activation analysis, *Journal of Radioanalytical and Nuclear Chemistry*, Vol. 301, 2014, pp. 811-819.
[22]. M. Mariscotti, A method for automatic identification of peaks in the presence of background and its application to spectrum analysis, *Nuclear Instruments and Methods*, Vol. 50, Issue 2, 1967, pp. 309-320.
[23]. GR1A gamma ray spectrometer (https://www.kromek.com/product/gamma-ray-detector-spectrometers-czt-based-gr-range/).
[24]. M. Prokesch, CdZnTe for gamma and x-ray applications, in Solid-State Radiation Detectors: Technology and Applications, S. Awadalla, Editor, *CRC Press*, 2015.
[25]. S1000 (https://www.dji.com/spreading-wings-s1000).
[26]. Pixhawk (http://pixhawk.org/).
[27]. S. Rizos, Network RTK research and implementation - a geodetic perspective, *Journal of Global Positioning Systems*, Vol. 1, Issue 2, 2002, pp. 144-150.
[28]. GPS/GNSS RTK technology (https://support.swiftnav.com/customer/en/portal/articles/2492803-understanding-gps-gnss-rtk-technology).
[29]. L1/L2 GPS/GLONASS Helix Antennas (https://www.maxtena.com/products/gps-glonass-l1-l2-antennas/).

Published by International Frequency Sensor Association (IFSA) Publishing, S. L., 2019 (http://www.sensorsportal.com).